A method using a density–energy state function with a reference equation of state for fluid-dynamics simulation of vapor–liquid–solid carbon dioxide

Morten Hammer, Åsmund Ervik, and Svend Tollak Munkejord*

SINTEF Energy Research, P.O. Box 4761 Sluppen, NO-7465 Trondheim, Norway

E-mail: Svend.T.Munkejord@sintef.no

Abstract

With the advent of CO_2 capture and storage (CCS) as an important remedy for reducing atmospheric CO_2 emissions, it has become necessary to develop accurate and efficient simulation tools. Among other things, such tools should handle the depressurization from supercritical pressures down to atmospheric conditions. This might involve the formation of solid CO_2 (dry ice) as the state passes the triple point. In this work, we propose a dynamic simulation method that handles the dry-ice formation. The method uses the Span–Wagner reference equation of state, with additional relations for thermodynamic properties along the sublimation line. A density–energy state function formulation is employed, which naturally follows from mass and energy conservation. To illustrate the method's capabilities, demanding test cases are considered, both for the depressurization of a vessel and for fluid dynamics in a pipeline, where phase change occurs due to changing boundary conditions.

*To whom correspondence should be addressed

Introduction

In Energy Technology Perspectives 2012,[1] the International Energy Agency (IEA) recommends CO_2 capture and storage (CCS) as one of the major means to reduce CO_2 emissions to the atmosphere. In the two-degree scenario (2DS), CCS accounts for $7\,\text{Gt}\,CO_2$ per year in 2050.[1] The points of capture will, to a large extent, not be colocated with the storage sites. Therefore, transportation in pipelines or in tanks will be necessary. Due to the large quantities of CO_2, it will be required to maintain a high level of safety while keeping the costs moderate. Herein, accurate simulation tools may help, during both design and operation.

One such safety issue is to avoid running fractures. If a pipeline ruptures, the crack may start to propagate, depending on the load on the pipe and the crack-propagation speed relative to the speed of the expansion wave in the fluid inside the pipe.[2,3] Simulating this requires accurate models for the structural mechanics and for the flow inside, and out of, the pipe. Recent computational studies indicate that CO_2 pipelines may be more susceptible to crack propagation than pipelines filled with natural gas.[4,5]

Another issue requiring modeling is the depressurization of pipelines. This can occur because of regular maintenance or an accident. Most often, the CO_2 inside the pipeline will be in a liquid or dense state. Depressurization will then entail phase change and a strong cooling. It is of interest to estimate the lowest temperature that may occur, since the temperature where some steel types become brittle may be reached. Reliable estimates of the lowest temperature may reduce over-engineering of pipelines and thus reduce costs. At the same time, such estimates may support the development of operational guidelines. Modeling issues regarding the transient simulation of pipeline transport of CO_2 mixtures were reviewed by Aursand et al..[6]

In dynamic simulations such as those performed here, the problem is commonly formulated using mass and energy balances. Thus, at each time step, we know the density ρ and the specific internal energy u. The remaining variables, such as pressure P and temperature T, must be determined from an equation of state (EOS). The fact that the latter variables (P, T) are unknown, and not input parameters, makes the problem challenging to solve. One approach is to exploit the

fact that the equilibrium condition represents a maximum in the entropy of the system.[7] Herein, the thermodynamically stable phases must be found, subject to the condition of constant volume and energy. As remarked by Giljarhus et al.,[8] this problem has been given limited attention in the literature, and then usually for multicomponent mixtures.[9–17]

Giljarhus et al.[8] studied the solution of the Span and Wagner[18] reference EOS (SW EOS) using a density–energy state function with application to dynamic simulations of depressurizations and fluid flow of pure CO_2. Their method was shown to be robust and efficient for various test problems. In particular, the equivalent routines in the REFPROP[19] program package were shown to be 15–20 times slower. However, Giljarhus et al. only considered the single-phase and two-phase (vapor–liquid) areas. For this reason, their calculations were limited to pressures above the triple-point pressure of CO_2 (518 kPa), at which the vapor–liquid–solid equilibrium needs to be considered. Depressurization of CO_2 from elevated pressures down to atmospheric conditions has considerable practical interest. Therefore, in this work, we propose a method to account for the occurrence of a solid phase in the density–energy framework discussed by Giljarhus et al..[8] This is done by employing the Clapeyron equation together with auxiliary functions for the density and pressure as functions of temperature along the sublimation line in the phase diagram. In this way, the solid properties are accounted for at the triple point and for the solid–vapor mixture. For dynamic simulations, we compare the SW EOS with the simple Peng and Robinson[20] (PR) cubic EOS. Using the PR EOS, we also illustrate the effect of ignoring the formation of a solid phase.

There are two known EOSs for solid CO_2, both enabling property calculations of dry ice. Trusler[21,22] published a Helmholtz-energy-based EOS, while Jäger and Span[23] presented a Gibbs-free-energy function. These EOSs can be used to solve equilibrium problems together with an EOS describing the liquid and vapor properties of CO_2. The methods of Trusler and Jäger and Span are thought to be accurate and general, but also more complex and somewhat more computationally expensive than the one we consider here. The present method may therefore be useful in situations where the main emphasis is on the fluid phases and computational efficiency is paramount.

Thermodynamics

Thermodynamic properties

If an expression for the Helmholtz free energy $a(T, \rho)$ is known along with its derivatives, all thermodynamic properties can be derived from these. T is temperature and ρ is the density. Here we are interested in pressure, enthalpy, entropy and internal energy, which can be obtained as follows:

$$P(T, \rho) = \rho^2 \left(\frac{\partial a}{\partial \rho} \right)_T, \tag{1}$$

$$s(T, \rho) = - \left(\frac{\partial a}{\partial T} \right)_\rho, \tag{2}$$

$$h(T, \rho) = a + \rho \left(\frac{\partial a}{\partial \rho} \right)_T - T \left(\frac{\partial a}{\partial T} \right)_\rho, \tag{3}$$

$$u(T, \rho) = a - T \left(\frac{\partial a}{\partial T} \right)_\rho. \tag{4}$$

It is common to define a reduced nondimensional Helmholtz function, $\phi = a/RT$, and to split the function in an ideal-gas part, ϕ^0, and a residual part, ϕ^r:

$$\phi(\tau, \delta) = \phi^0(\tau, \delta) + \phi^r(\tau, \delta). \tag{5}$$

The variables used for the nondimensional Helmholtz function are the inverse reduced temperature, $\tau = T_{crit}/T$, and the reduced density $\delta = \rho/\rho_{crit}$. T_{crit} is the critical temperature and ρ_{crit} is the critical density.

The Span–Wagner reference equation of state for CO_2

The Span–Wagner reference equation of state for CO_2 (SW EOS) is in the reduced Helmholtz form of eq 5. The Helmholtz function and its derivatives are found in the original paper by Span and Wagner.[18] It contains a total of 51 terms, including logarithms and exponentials, making it computationally demanding. Efficient numerical methods are therefore required to maintain a
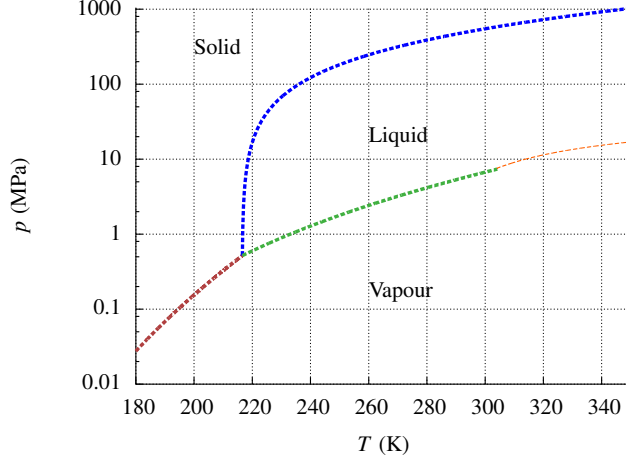
Figure 1: Phase diagram for CO_2.

reasonable run time for a dynamics simulation.

The SW EOS is valid from the triple-point temperature to $1100\,K$ and for pressures up to $800\,MPa$. Span and Wagner also provided auxiliary equations for the sublimation line and the fusion line. These equations are used together with the saturation line calculated from the Helmholtz function for pure CO_2 to plot the phase diagram in Figure 1. The dotted line continuing the saturation line above the critical pressure and temperature represents $(\partial^2 P/\partial\rho^2)_T = 0$. The triple point and critical properties of CO_2 are displayed in Table 1.

In this work, we assume that the SW EOS is valid for vapor-phase properties below the triple-point temperature.

Table 1: Critical properties of CO_2. Data taken from Span and Wagner,[18] except for the solid density at the triple point, which is calculated from eq 7.

Property	Symbol	Value
Critical density	ρ_{crit}	$467.6\,kg/m^3$
Critical temperature	T_{crit}	$304.1282\,K$
Critical pressure	P_{crit}	$7.3773\,MPa$
Triple-point temperature	T_{tr}	$216.592\,K$
Triple-point pressure	P_{tr}	$0.51795\,MPa$
Triple-point density		
liquid	$\rho_{tr,\ell}$	$1178.5\,kg/m^3$
vapor	$\rho_{tr,v}$	$13.761\,kg/m^3$
solid	$\rho_{tr,s}$	$1511.6\,kg/m^3$

The SW EOS is tuned against a large set of experimental data for single-phase properties, that is, the liquid–vapor saturation line, speed of sound, specific isobaric heat capacity, specific isochoric heat capacity, specific enthalpy, specific internal energy and the Joule–Thompson coefficient. The uncertainty of the EOS is estimated to be less than 0.05% for the density, less than 1.0% for the speed of sound and less than 1.5% for the specific isobaric heat capacity. [18]

Dry-ice modeling

To simulate the appearance of dry ice, we must extend the thermodynamic model to include solid properties for the triple point and to account for a mixture of solid and vapor. These properties can be calculated by applying the Clapeyron equation. Two-phase solid–liquid does not need to be modeled, since it will not occur at normal operating conditions of vessels and pipelines. It is also not possible to get two-phase solid–liquid from a homogeneous isentropic decompression from single-phase liquid or vapor, which is the primary interest of this paper. For the same reasons, there is no need for modeling a pure solid.

It might, however, be possible to get into two-phase solid–liquid during a depressurization, if the phases are allowed to separate. The cooling of the fluid can then be greater than the pure isentropic cooling of the depressurization. For the homogeneous systems considered here, on the other hand, any deviation from isentropic behavior will reduce the cooling.

In view of the above, we model dry ice at the sublimation line, that is, solid CO_2 in equilibrium with vapor. This can be achieved using the Clapeyron equation,

$$\left(\frac{\mathrm{d}P}{\mathrm{d}T}\right)_{\text{subl}} = \frac{\Delta h_{\text{subl}}}{T\Delta v_{\text{subl}}} = \frac{h_{\text{v}} - h_{\text{s}}}{T\left(v_{\text{v}} - v_{\text{s}}\right)}. \tag{6}$$

From eq 6, it is seen that the solid enthalpy at the sublimation line can be calculated if the derivative of pressure with respect to temperature, $(\mathrm{d}P/\mathrm{d}T)_{\text{subl}}$, and the specific solid volume, v_{s}, are known, together with the vapor properties from the SW EOS.

Table 2: Coefficients used for the solid-density correlation.

Parameter	Value	Unit
A	-0.0224	$\mathrm{kg/m^3K^2}$
B	6.8896	$\mathrm{kg/m^3K}$
C	1070.8	$\mathrm{kg/m^3}$

Table 3: Coefficients used for the sublimation-pressure correlation.

i	a	b
0	-14.7408463	1.0
1	2.4327015	1.9
2	-5.3961778	2.9

The solid density can be modeled as a polynomial in terms of the temperature,

$$\rho_{\mathrm{s}}(T) = AT^2 + BT + C, \tag{7}$$

where a set of polynomial coefficients are given in Table 2. This polynomial has been fitted to data tabulated by Höchst [24] for CO_2 properties along the sublimation line from 193.15 K up to the triple-point temperature. As already mentioned, Span and Wagner [18] published an auxiliary function for the sublimation pressure $P_{\mathrm{subl}}(T)$:

$$P_{\mathrm{subl}} = P_{\mathrm{tr}} \exp\left(\frac{B(\tau_{\mathrm{tr}})}{\tau_{\mathrm{tr}}}\right), \tag{8}$$

$$B(\tau_{\mathrm{tr}}) = \sum_{i=0}^{2} a_i (1 - \tau_{\mathrm{tr}})^{b_i}. \tag{9}$$

Here $\tau_{\mathrm{tr}} = T/T_{\mathrm{tr}}$ is the reduced temperature, and the coefficients a and b are listed in Table 3. The required derivative $(\mathrm{d}P/\mathrm{d}T)_{\mathrm{subl}}$ is found by differentiating eqs 8 and 9. The function describing the sublimation pressure is validated against experimental data from 180 K to the triple point. [18]

When Δh_{subl} and Δv_{subl} are known, both the internal energy and entropy of dry ice at the
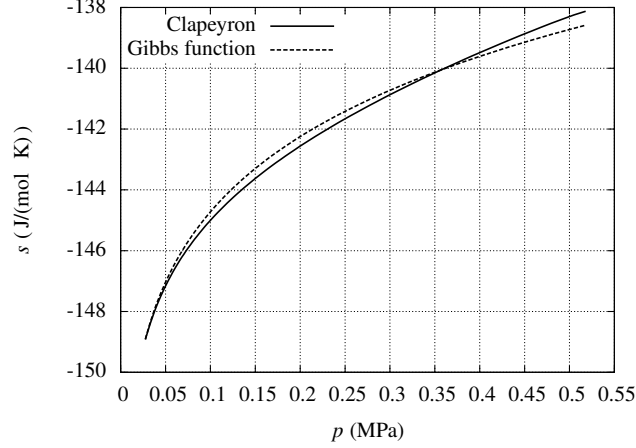
Figure 2: Entropy, s (J/(mol K)), along the sublimation line plotted with the Clapeyron method, and by using the Gibbs-free-energy function published by Jäger and Span.[23]

sublimation line can be calculated using the following thermodynamic relations:

$$u_s = u_v - \Delta h_{subl} + P \Delta v_{subl}, \tag{10}$$

$$s_s = s_v - \frac{\Delta h_{subl}}{T}. \tag{11}$$

Using the same approach, it is possible to calculate the dry-ice properties along the fusion line. This is not considered in further detail here.

It is also possible to calculate the properties of solid CO_2 using the EOS for solid carbon dioxide based on the Gibbs free energy published by Jäger and Span[23] or the Helmholtz-energy function of Trusler.[21] These are more general approaches that also can be used for multicomponent mixtures and other EOSs. For the present work, where only dry ice at the sublimation line needs to be described, it is sufficient to model the dry ice using the Clapeyron equation.

Only limited experimental data for the thermodynamic properties of solid CO_2 are available, but the Gibbs-free-energy function by Jäger and Span[23] represents most of the available data to experimental uncertainty. The proposed model, applying the Clapeyron equation, is validated by plotting the entropy against that obtained using the Gibbs-free-energy function of Jäger and Span[23] in Figure 2. The observed difference is considered to be insignificant in the present context.
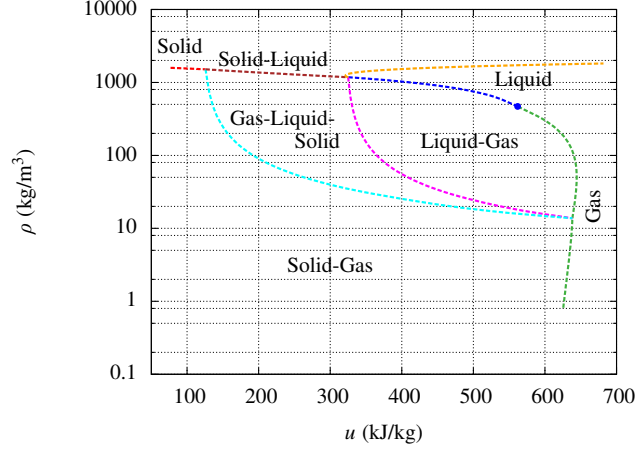
8

Figure 3: Phase diagram for CO_2 in the (ρ, u) plane. The circular dot marks the critical point.

Equilibrium and the ρu problem

During resolution of the conservation equations for a vessel model or for a fluid element in a pipe simulation, the overall mass and energy is integrated forward in time. For the governing system of equations considered here, the specific internal energy can be calculated from the total energy. Here, the specific mass, ρ_{in}, and specific internal energy, u_{in}, are given, denoted by the subscript in, and the pressure, P, temperature, T, and phase mass fractions, z_v, z_ℓ and z_s, must be calculated. This is the ρu problem.

The densities and specific internal energies along the saturation line, sublimation line, fusion line (not dry ice) and for the coexistence region of vapor, liquid and solid are plotted in Figure 3. It is seen that the triple point of the temperature-pressure space occupies a large region of the ρu space.

Different problem formulations are required for all the different areas shown in Figure 3. The single-phase equation is the simplest, being simply

$$u(T, \rho_{in}) - u_{in} = 0, \tag{12}$$

where ρ_{in} and u_{in} are the specified ρ and u. Equation 12 must be solved for the unknown temperature, T.

9

To solve the ρu problem for liquid in equilibrium with vapor, both the equilibrium conditions $P_v = P_\ell$, $G_v = G_\ell$ and the density and internal energy specification equations must be fulfilled:

$$P(T, \rho_v) - P(T, \rho_\ell) = 0, \tag{13}$$

$$G(T, \rho_v) - G(T, \rho_\ell) = 0, \tag{14}$$

$$z_v u(T, \rho_v) + (1 - z_v) u(T, \rho_\ell) - u_{in} = 0, \tag{15}$$

$$\frac{z_v}{\rho_v} + \frac{(1 - z_v)}{\rho_\ell} - \frac{1}{\rho_{in}} = 0. \tag{16}$$

Here $G(T, \rho)$ denotes the Gibbs free energy. The unknowns of the liquid–vapor equation system, eqs 13–16, are $[\rho_v, \rho_\ell, T, z_v]$.

In the pressure–temperature plane triple point (T_{tr}, P_{tr}), vapor, liquid and solid CO_2 are in equilibrium. Solving the ρu problem at this point means solving three algebraic equations,

$$z_v u_{tr,v} + z_\ell u_{tr,\ell} + z_s u_{tr,s} - u_{in} = 0, \tag{17}$$

$$\frac{z_v}{\rho_{tr,v}} + \frac{z_\ell}{\rho_{tr,\ell}} + \frac{z_s}{\rho_{tr,s}} - \frac{1}{\rho_{in}} = 0, \tag{18}$$

$$z_v + z_\ell + z_s - 1 = 0. \tag{19}$$

The unknowns of the triple-point equation system, eqs 17–19, are $[z_v, z_\ell, z_s]$.

At the sublimation line the equilibrium condition simplifies to two pressure equations, $P = P_{subl}(T) = P(T, \rho_v)$,

$$P - P_{subl}(T) = 0, \tag{20}$$

$$P - P(T, \rho_v) = 0, \tag{21}$$

$$z_v u(t, \rho_v) + (1 - z_v) u_s - u_{in} = 0, \tag{22}$$

$$\frac{z_v}{\rho_v} + \frac{(1 - z_v)}{\rho_s} - \frac{1}{\rho_{in}} = 0. \tag{23}$$

The unknowns of the sublimation ρu problem, eqs 20–23, are $[P, \rho_v, T, z_v]$.

The ρu algorithm

Given $(\rho_{\text{in}}, u_{\text{in}})$, a qualified guess for the correct phase will simplify the ρu problem. Otherwise, all the different phase combinations would have to be tried in order to find the solution.

The following four criteria are used to determine which phases to solve for:

1. Since the triple-point ρu problem is three algebraic equations, it is simple to solve these equations. A valid solution is $z_{\text{v}} \geq 0$, $z_{\ell} \geq 0$ and $1 - z_{\text{v}} - z_{\ell} \geq 0$.

2. Another simple test is to check if the solution lies above or below the line made between the two points $(u_{\text{tr,v}}, v_{\text{tr,v}})$ and $(u_{\text{tr},\ell}, v_{\text{tr},\ell})$ in the uv space. If the specification is above the line, the solution will be either in the single-phase area or in the liquid–vapor area. If the specification is below the line, the solution will be either single-phase vapor or a mixture of solid and vapor.

3. Giljarhus et al.[8] used a polygon representing the inside of the liquid–vapor (ρ, u) space area, together with a ray-crossing algorithm, to determine whether a point was in the liquid–vapor region. The same criterion is used here.

4. A polygon can be mapped for the vapor properties at the sublimation line. It is possible to determine if the specified point, $(\rho_{\text{in}}, u_{\text{in}})$, lies to the left or to the right of the polygon, by calculating a cross product for each line segment of the polygon.

The second criterion determines whether the third or the fourth criterion applies. Note that the first two criteria are exact, while the two latter may fail, because of the difference between the polygons and the actual nonlinear functions. If they fail, a second guess is made. This second guess will always succeed, since the third and fourth criteria are binary choices; a point is either inside or outside the vapor–liquid region, and a point is either to the left or to the right of the sublimation line.

The ρu problem is solved using a Newton-Raphson numerical solver combined with a line search to guarantee convergence, cf. Chapter 6 of Dennis and Schnabel.[25] Analytical Jacobians are provided for all the different problem formulations, allowing for efficient solution of the equations.

For the method to be robust, the liquid–vapor and solid–vapor ρu problems must be solved in a nested manner.[15] For the liquid–vapor case, the equilibrium conditions, eqs 13 and 14, are solved in the inner loop, and the modified internal energy and density equations are solved in the outer loop,

$$\frac{z_v u(T, \rho_v) + (1 - z_v) u(T, \rho_\ell) - u_{\text{in}}}{1000T} = 0, \tag{24}$$

$$\frac{z_v \rho_{\text{in}}}{\rho_v} + \frac{(1 - z_v) \rho_{\text{in}}}{\rho_\ell} - 1 = 0. \tag{25}$$

The above are scaled versions of eqs 15 and 16, in order to minimize numerical errors.

For the solid–vapor ρu problem, the pressure eqs 20 and 21 are solved in the inner loop, and the modified internal energy and density equations are solved in the outer loop,

$$\frac{z_v u(t, \rho_v) + (1 - z_v) u_s - u_{\text{in}}}{1000T} = 0, \tag{26}$$

$$\frac{z_v \rho_{\text{in}}}{\rho_v} + \frac{(1 - z_v) \rho_{\text{in}}}{\rho_s} - 1 = 0. \tag{27}$$

Again, eqs 22 and 23 are scaled in order to minimize numerical errors.

For the liquid–vapor and solid–vapor systems, the mass fraction z_v of the vapor must lie between 0 and 1. Similarly, the temperature T of the liquid–vapor system must be between T_{tr} and T_{crit}, and the temperature of the solid–vapor system must be $T \leq T_{\text{tr}}$. This implies that the liquid–vapor and solid–vapor equation systems will provide either a valid solution or no solution at all.

For the single-phase ρu problem, there is, unfortunately, no such sanity check. Solving eq 12 might produce a metastable liquid or vapor phase. The solution therefore has to be checked for phase stability by comparing the solution pressure against either the saturation or the sublimation pressure, depending on the solution temperature.

The Ps problem

In a pipeline depressurization simulation, for subsonic flow, it is desirable to apply a boundary condition for the pressure, P. From the inner domain, we extrapolate the mass flux, ρw and entropy,
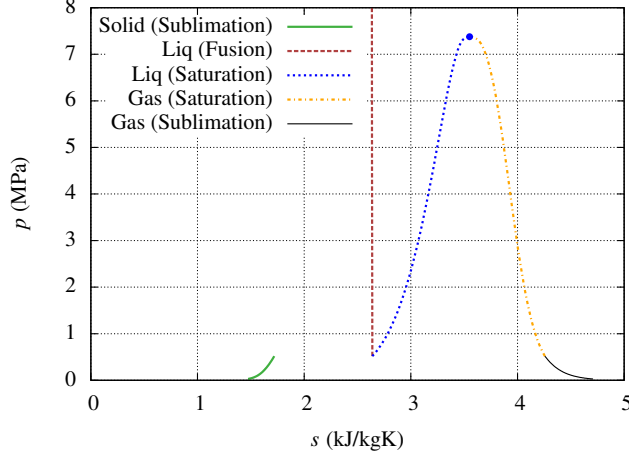
Figure 4: Phase diagram for CO_2 in the (p, s) plane.

s. The entropy is chosen since it is a characteristic variable of the Euler equations; see eqs 39–41 below. As a result of this, temperature and phase mass fractions must be calculated from pressure and entropy. This is the Ps problem.

The dry-ice entropy at the sublimation line is calculated from eqs 6 and 11. The vapor and liquid entropies are calculated from the SW EOS. The pressure is plotted against entropy in Figure 4.

A different problem formulation is required for all the different phase combinations shown in Figure 4. The single-phase Ps problem must satisfy two nonlinear equations,

$$P(T, \rho) - P_{\text{in}} = 0, \tag{28}$$

$$s(T, \rho) - s_{\text{in}} = 0. \tag{29}$$

The unknowns are $[T, \rho]$.

The liquid–vapor Ps problem can be solved in two steps. First, the equilibrium temperature at the specified pressure, P_{in}, is found by solving eqs 13 and 14. When the temperature and the phase densities at the saturation line are known, the liquid–vapor Ps problem is reduced to a single algebraic equation,

$$z_{\text{v}} s(T, \rho_{\text{v}}) + (1 - z_{\text{v}}) s(T, \rho_{\ell}) - s_{\text{in}} = 0, \tag{30}$$

for the unknown vapor phase fraction, z_{v}.

13

The solid–vapor Ps problem can be solved in three steps. The first step is finding the sublimation temperature for the given pressure by solving

$$P_{in} - P_{subl}(T) = 0. \tag{31}$$

The second step is solving the SW EOS for the vapor density, ρ_v, at the sublimation line,

$$P(T, \rho_v) - P_{in} = 0. \tag{32}$$

Finally, the vapor mass fraction, z_v, can be found by solving the linear algebraic equation

$$z_v s_v + (1 - z_v) s_s - s_{in} = 0. \tag{33}$$

The Ps problem does not always have a unique solution for the triple-point pressure. The equation system for the triple point is given by

$$z_v s_{tr,v} + z_\ell s_{tr,\ell} + (1 - z_v - z_\ell) s_{tr,s} - s_{in} = 0$$
$$P - P_{tr} = 0. \tag{34}$$

When $s_{tr,s} < s_{in} < s_{tr,v}$, multiple combinations of z_v and z_ℓ will satisfy the specification equation. This can also be seen from Figure 4.

The Ps algorithm

The single-component Ps problem is easy to solve when compared to the ρu problem. Given the pressure, there are four possibilities.

1. $P \geq P_{crit}$: Single-phase solution.

2. $P_{tr} < P < P_{crit}$: Single-phase or liquid–vapor solution. The entropies s_v and s_ℓ at the saturation line are used to determine if the solution is single-phase or two-phase liquid–vapor.

14

3. $P = P_{tr}$: Single-phase vapor or no unique solution.

4. $P < P_{tr}$: Single-phase vapor solution, or solid–vapor solution. The entropies s_v and s_s at the sublimation line are used to determine if the solution is single-phase vapor or two-phase solid–vapor.

The Peng–Robinson equation of state

To illustrate some of the benefits of using a multiparameter equation of state, a comparison with the Peng and Robinson[20] equation of state (PR EOS) is included. Some selected properties are plotted against the saturation pressure in Figure 5. It is seen that the SW and PR EOS saturation temperatures as a function of pressure are similar. The liquid density and liquid speed of sound deviate significantly, and the vapor speed of sound deviates in the proximity of the critical point.

In order to solve the ρu and Ps problems using the PR EOS, the same strategy as that for the SW EOS is employed. The sublimation-line function in eq 8 is utilized by shifting the triple-point temperature to meet the saturation line at $P_{tr} = 0.51795\,\text{MPa}$. The main difference is the variables used during resolution. The PR EOS and its differentials are evaluated and solved for temperature and pressure, (T, P), not temperature and density, (T, ρ), as for the SW EOS.

Vessel model

To perform a depressurization simulation of a vessel, we formulate a model employing the following dynamic conservation equations for mass and energy:
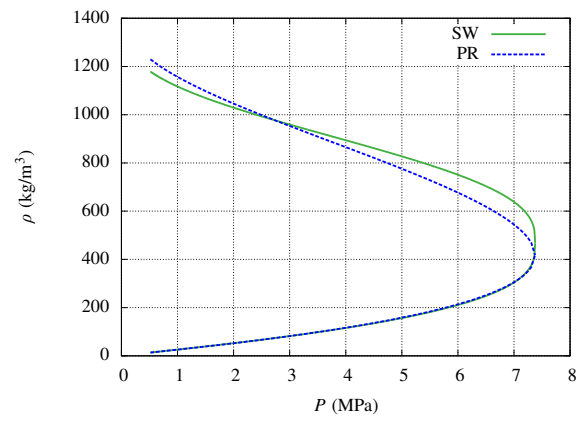
$$\frac{\mathrm{d}M}{\mathrm{d}t} = -\dot{m}(P, \rho), \tag{35}$$

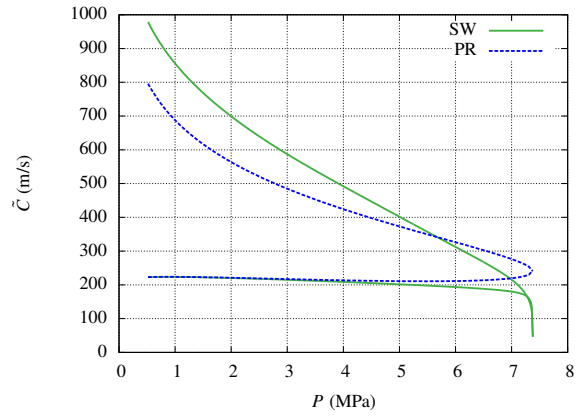$$\frac{\mathrm{d}U}{\mathrm{d}t} = \dot{Q}(T) - \dot{m}(P, \rho)h(T, \rho). \tag{36}$$

Here, M is the total mass in the vessel, $\dot{m}$ is the mass-flow rate, U is the internal energy and $\dot{Q}$ is the heat-transfer rate. The vessel is treated as a rigid body with constant volume, V. The specific

15
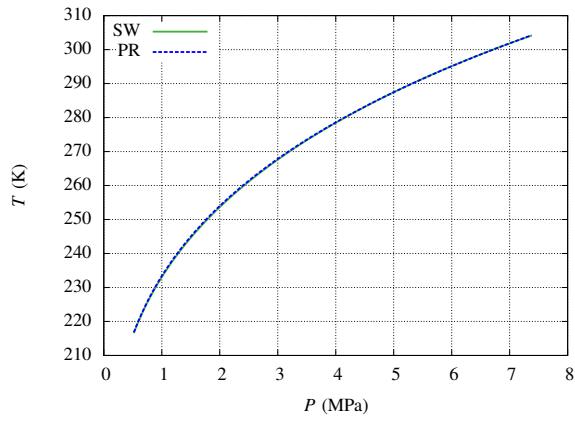
(a) Saturation temperature

(b) Density along the saturation line

(c) Single-phase speed of sound along the satura-
tion line

Figure 5: Temperature, T, density, ρ, and single-phase speed of sound, $\tilde{C}$, plotted against pressure along the saturation line for the SW and PR EOS.
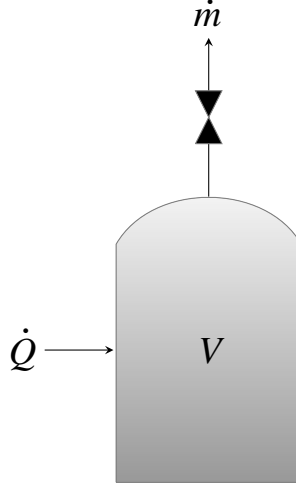
Figure 6: Schematic illustration of the vessel model.

internal energy and density are related to the conserved variables as $u = U/M$ and $\rho = M/V$, and the solver for the ρu problem described above is used to calculate the pressure, temperature and phase mass fractions of the vessel. The vessel model is illustrated in Figure 6.

To have closure of the vessel model, we need expressions for the heat-transfer rate, $\dot{Q}$, and the mass-flow rate, $\dot{m}$. The heat transfer is modeled as a heat-transfer rate multiplied with the difference between the vessel temperature, T, and the ambient temperature, T_{amb},

$$\dot{Q}(T) = \eta A \left(T_{\mathrm{amb}} - T\right), \tag{37}$$

where η (W/m^2 K) is the overall heat-transfer coefficient and A is the surface area of the vessel. The flow rate is modeled using a simplified valve equation,

$$\dot{m} = K_{\mathrm{v}}\sqrt{\rho \left(P - P_{\mathrm{amb}}\right)}, \tag{38}$$

where K_{v} (m^2) is a flow coefficient for the valve and P_{amb} is the ambient pressure. To integrate the equations, the DASSL[26] differential-algebraic equation solver is used.

There exist experimental results from vessel depressurization.[27,28] However, a direct comparison to the measured temperature, pressure and void fraction at different vertical positions in the vessel

would require a substantial extension of the vessel model presented here.

Fluid dynamics

Governing equations

Another typical application of the above thermodynamic algorithms is in a 1D flow model, in which CO_2 may undergo a phase change. For simplicity, we assume that all the phases have the same velocity, such that the governing equations have the same form as the Euler equations for single-phase flow:

$$\frac{\partial(\rho)}{\partial t} + \frac{\partial(\rho w)}{\partial x} = 0, \tag{39}$$

$$\frac{\partial(\rho w)}{\partial t} + \frac{\partial(P + \rho w^2)}{\partial x} = 0, \tag{40}$$

$$\frac{\partial(\rho e)}{\partial t} + \frac{\partial[w(\rho e + P)]}{\partial x} = 0. \tag{41}$$

Here, $\rho = \alpha_\ell \rho_\ell + \alpha_v \rho_v + \alpha_s \rho_s$ is the mixture density, w is the velocity and $e = u + 1/2 w^2$ is the specific total energy. This model can be regarded as a drift-flux model with no slip (no relative velocity) between the phases, and it is often denoted as the *homogeneous equilibrium* model. It can be accurate if the interphasic momentum transfer is high, such as in highly dispersed flows.

In this work, the purpose is to illustrate the ρu problem. Therefore, we neglect other physical effect, such as wall friction, heat transfer and gravity. These effects could be included in the above equation system as source terms.

When the thermodynamic relation, $de = T\,ds + P/\rho^2\,d\rho$, is applied on the fluid eqs 39–41, it can be shown that the specific entropy, s, is advected with the flow,

$$\frac{\partial s}{\partial t} + w\frac{\partial s}{\partial x} = 0. \tag{42}$$

Hence, it follows that if the initial specific entropy is constant in the pipe, the specific entropy will

remain constant for a pipe with no inflow.

Numerical method

The governing eqs 39–41 are discretized using the finite-volume method. They are then solved numerically using the first-order centered (FORCE) scheme.[29] It is optimal in the sense that it has the least numerical dissipation of the first-order central schemes that are stable for all Courant–Friedrichs–Lewy (CFL) numbers less than unity.[30]

The FORCE scheme is also the building block of the multistage centered scheme (MUSTA) by Toro and coworkers.[31,32] This scheme aims at attaining the accuracy of upwind schemes while retaining much of the simplicity of centered schemes. It has been employed for several two-phase flow models, including drift-flux models.[33,34]

The system of eqs 39–41 can be written in the following form:

$$\frac{\partial \boldsymbol{q}}{\partial t} + \frac{\partial \boldsymbol{f}(\boldsymbol{q})}{\partial x} = \boldsymbol{0}, \tag{43}$$

where $\boldsymbol{q} = [\rho, \rho w, \rho e]^{\top}$ is the vector of conserved variables. Employing the finite-volume method, we obtain the discretized system

$$\boldsymbol{q}_j^{m+1} = \boldsymbol{q}_j^m - \frac{\Delta t}{\Delta x}\left(\boldsymbol{f}_{j+1/2}^m - \boldsymbol{f}_{j-1/2}^m\right), \tag{44}$$

where $\boldsymbol{q}_j^m$ denotes the numerical approximation to the cell average of the vector of unknowns $\boldsymbol{q}(x, t_m)$ in control volume j at time step m. In the FORCE scheme, the numerical flux at the cell interface at $x_{j+1/2}$ is a function of the cell averages on each side:

$$\boldsymbol{f}_{j+1/2} = \boldsymbol{f}^{\mathrm{FORCE}}(\boldsymbol{q}_j, \boldsymbol{q}_{j+1}). \tag{45}$$

To obtain second-order spatial accuracy, we employ a semidiscrete version of the monotone upwind-centered scheme for conservation laws (MUSCL).[35,36] Herein, a piecewise linear function

19

is constructed by using the data $\{q_j(t)\}$. At each side of the interface $x_{j+1/2}$ we have values from the linear approximations in the neighboring cells. These are denoted by

$$q_j^R = q_j + \frac{\Delta x}{2} l_j \quad \text{and} \quad q_{j+1}^L = q_{j+1} - \frac{\Delta x}{2} l_{j+1}, \tag{46}$$

where l_j are the slopes calculated using a suitable slope-limiter function. There are several possible choices of variables to use in the slope-limiter procedure. Here we have chosen the variables (w, ρ, u). After this procedure, the numerical flux is found from

$$f_{j+1/2} = f^{\text{FORCE}}(q_j^R, q_{j+1}^L). \tag{47}$$

For use with the MUSCL scheme, the system of conservation equations, eq 43, is semidiscretized:

$$\frac{dq_j}{dt} = -\frac{f_{j+1/2} - f_{j-1/2}}{\Delta x}. \tag{48}$$

To obtain a second-order solution in time, we employ the two-stage second-order strong-stability-preserving (SSP) Runge–Kutta (RK) method (see, for instance, Ketcheson and Robinson[37]).

Mixture speed of sound

In the numerical method, eq 44, the time-step length is restricted by the Courant–Friedrichs–Lewy (CFL) stability criterion, given by the CFL number

$$R = \frac{\|\lambda\|_\infty \Delta t}{\Delta x}, \tag{49}$$

where $\|\lambda\|_\infty$ is the maximum value in the computational domain of the eigenvalues of the Jacobian matrix of the flux function f in eq 43. Here, we have

$$\|\lambda\|_\infty = \max|w \pm \tilde{C}|, \tag{50}$$

20

where $\tilde{C}$ is the speed of sound. It should be noted that, outside the single-phase region, the predicted speed of sound of the mixture is not a purely thermodynamic function, but it is the combined result of thermodynamic relations employed in the flow model. Furthermore, the equilibrium assumptions made regarding pressure, velocity and chemical potential will influence the speed of sound. This is discussed by Flåtten and Lund[38] and Lund.[39]

Vapor–liquid

In the vapor–liquid region, the mixture speed of sound $\tilde{C}_{v,\ell}$ for the present homogeneous equilibrium flow model can be calculated e.g. as shown in Section 9.2.1 in the paper of Lund:[39]

$$\tilde{C}_{v,\ell}^{-2} = \rho(Z_p + Z_{pT} + Z_{pT\mu}), \tag{51}$$

$$Z_p = \frac{\alpha_g}{\rho_g c_g} + \frac{\alpha_l}{\rho_l c_l}, \tag{52}$$

$$Z_{pT} = \frac{c_{p,g} c_{p,l} T}{c_{p,g} + c_{p,l}} \left(\frac{\Gamma_l}{\rho_l c_l} - \frac{\Gamma_g}{\rho_g c_g} \right)^2, \tag{53}$$

$$Z_{pT\mu} = \frac{\rho_{\mathrm{mix}} T}{c_{p,g} + c_{p,l}} \left(\frac{\rho_g - \rho_l}{\rho_g \rho_l (h_g - h_l)} (c_{p,g} + c_{p,l}) + \frac{\Gamma_g c_{p,g}}{\rho_g \tilde{C}_g^2} + \frac{\Gamma_l c_{p,l}}{\rho_l \tilde{C}_l^2} \right)^2, \tag{54}$$

where Γ_i is the Grüneisen coefficient,

$$\Gamma_i = \frac{1}{\rho_i} \left(\frac{\partial p}{\partial u_i} \right)_{\rho_i}. \tag{55}$$

It is interesting to note that, in large parts of the two-phase region, the mixture speed of sound is lower than the pure-vapor or pure-liquid speed of sound.

Vapor-solid

To calculate the speed of sound of a mixture of solid and vapor in equilibrium, we do not have expressions of the type in eqs 51–54 at hand. Instead, we consider the function

$$\boldsymbol{g}(\boldsymbol{y}(\rho_{\text{in}}), \rho_{\text{in}}) = \begin{bmatrix} P(T, \rho_{\text{v}}) - P \\ P_{\text{sub}}(T) - P \\ z_{\text{v}} s(T, \rho_{\text{v}}) + (1 - z_{\text{v}}) s_{\text{s}}(T, \rho_{\text{v}}) - s_{\text{in}} \\ \dfrac{z_{\text{v}}}{\rho_{\text{v}}} + \dfrac{(1 - z_{\text{v}})}{\rho_{\text{s}}(T)} - \dfrac{1}{\rho_{\text{in}}} \end{bmatrix}, \tag{56}$$

with

$$\boldsymbol{y}(\rho_{\text{in}}) = [P, \rho_{\text{v}}, T, z_{\text{v}}]^{\top}. \tag{57}$$

We require that the vapor and solid pressures be equal, and that the mixture entropy and volume be constant:

$$\boldsymbol{g}(\boldsymbol{y}(\rho_{\text{in}}), \rho_{\text{in}}) = \boldsymbol{0}. \tag{58}$$

Differentiating eq 58 with respect to the specified density ρ_{in} gives

$$\frac{\mathrm{d}\boldsymbol{g}}{\mathrm{d}\rho_{\text{in}}} = \frac{\partial \boldsymbol{g}}{\partial \boldsymbol{y}} \frac{\partial \boldsymbol{y}}{\partial \rho_{\text{in}}} + \frac{\partial \boldsymbol{g}}{\partial \rho_{\text{in}}} = \boldsymbol{0}. \tag{59}$$

The equation system (59) is set up using analytical derivatives, and solved for $\partial \boldsymbol{y}/\partial \rho_{\text{in}}$. The first element of the vector will be $\partial P/\partial \rho_{\text{in}}$ at constant entropy, whose square root is the speed of sound.
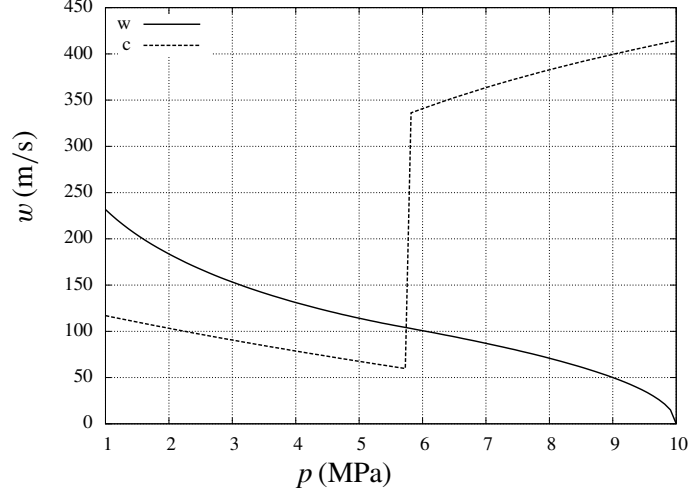
Figure 7: The fluid velocity calculated from the Bernoulli equations, and the mixture speed of sound, plotted against pressure.

Boundary conditions

The boundary pressure at the open end of the pipe is found by solving the steady-state version of the Euler equations, the Bernoulli equations for constant pipe cross section,

$$\mathrm{d}h + w\,\mathrm{d}w = 0, \tag{60}$$

$$\mathrm{d}s = 0, \tag{61}$$

$$\mathrm{d}(w\rho) = 0. \tag{62}$$

The Bernoulli equations are solved for the choke pressure, where the flow velocity equals the speed of sound, $w = \tilde{C}$. The solution of this equation system is illustrated in Figure 7, for an initial condition of $P = 100\,\mathrm{bar}$, $T = 300\,\mathrm{K}$ and $w = 0\,\mathrm{m/s}$. In this case, the solution is found at the discontinuity of the mixture speed of sound. The speed of sound is discontinuous across the phase boundaries.

It should be noted that, even if the Ps problem does not have a unique solution for the triple-point pressure, the Bernoulli equations have a unique path through the triple point. From the

thermodynamic identity for the enthalpy differential,

$$\mathrm{d}h = T\,\mathrm{d}s + v\,\mathrm{d}P, \tag{63}$$

it is seen that the Bernoulli path through the triple point is both constant entropy and constant enthalpy.

Results

In this section, the versatility of the proposed method is demonstrated by simulating a depressurization of a vessel, and by two challenging pipeline flow simulations in which the state dynamically changes between one, two and three phases. Flow problems are particularly challenging for the thermodynamic routines with respect to robustness and consistency. Further, these simulations will illustrate how all the thermodynamic variables are coupled through the fluid-flow model. In order to highlight the effect of the EOS, we consider idealized cases without including models for velocity slip, friction and heat transfer.

Vessel depressurization

As a test case, we consider a cylindrical tank with diameter $0.2\,\mathrm{m}$ and height $1.0\,\mathrm{m}$, with initial state $P_0 = 100\,\mathrm{bar}$ and $T_0 = 300\,\mathrm{K}$. The ambient conditions are $P_{\mathrm{amb}} = 1\,\mathrm{bar}$ and $T_{\mathrm{amb}} = 293.15\,\mathrm{K}$. A moderate overall heat-transfer coefficient of $\eta A = 1\,\mathrm{W/K}$ is used, and the valve coefficient is set to $K_{\mathrm{v}} = 5 \times 10^{-7}\,\mathrm{m}^2$. At $t = 0$, the valve is opened to the surroundings. Note that initially, CO_2 is in a liquid state, above the critical pressure, while at steady state, it will reach ambient conditions, which is in the vapor region. This is a challenging test case, since it covers pure liquid, transition to liquid–vapor, coexistence of vapor, liquid and solid at the triple point, transition to solid–vapor and finally transition to pure vapor.

   Figure 8 shows the main results from the vessel depressurization simulation. Pressure, tempera-
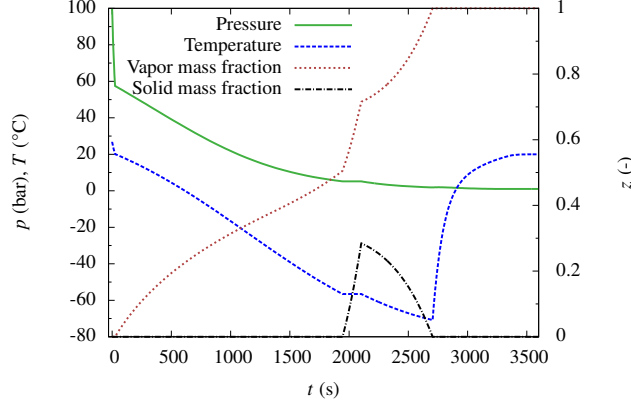
Figure 8: Depressurization of a vessel. Pressure (bar) and temperature (°C) are plotted along the left ordinate axis. Mass fractions of solid $(- \cdot -)$ and vapor $(\cdots)$ are plotted along the right ordinate axis.

ture and mass fractions are plotted against simulation time. The pressure and temperature drop fast down to the saturation line, and evaporation starts at approximately 59 bar. The process follows the saturation line down to the triple point. From the solid mass fraction, it is seen that the triple point is reached at approximately time $t = 1950$ s. The pressure and temperature then stay constant for approximately 150 s before leaving the triple point and continuing along the sublimation line. The solid then starts to sublimate. After approximately 2700 s, all the solid CO_2 has sublimated, and pure vapor remains. The temperature then rises quickly to ambient temperature.

The simulation trajectory is plotted in the ρu and PT space, see Figures 9a and 9b. The phase changes in the vessel during the simulations are clearly seen in both figures.

A comparison between the SW and PR EOS for the vessel simulation is shown in Figure 10. The dynamic trends from the SW and PR EOS simulations are similar, but the depressurization time for the PR EOS is shorter than that for the SW EOS.

Shock tube

The next test case is a Riemann problem (shock tube) and has been constructed to illustrate the wave separation at the phase boundaries and at the triple point. The physical interpretation of this case is a 100 m pipe section with two adjacent uniform states separated by a membrane. At time $t = 0$, the membrane ruptures, and waves will start to propagate. Initially, the fluid is at rest. The

25

(a) Trajectory in the ρu space.

(b) Trajectory in the TP space.
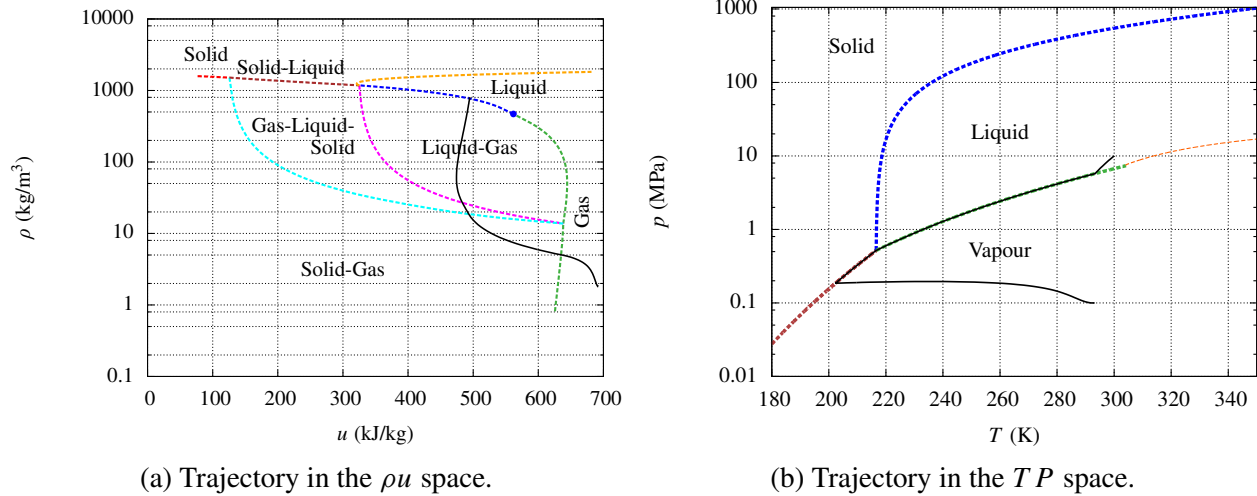
Figure 9: The vessel depressurization trajectory plotted in the ρu and the TP spaces, shown as a full black line. The circular dot in Figure (a) marks the critical point.

left half of the tube is at $250\,\text{K}$ and $3\,\text{MPa}$ (liquid phase), and the right half of the tube is at $250\,\text{K}$ and $0.1\,\text{MPa}$ (vapor phase).

The following fluid-dynamics simulations have been performed with the MUSCL-FORCE scheme employing the minmod limiter, see e.g. Sec. 9.2 in the book of LeVeque,[40] and a CFL number of 0.5. The case is simulated until $t = 0.06\,\text{s}$, and pressure, temperature, velocity, vapor volume fraction and solid volume fraction profiles are plotted for the end time. The numerical scheme has been shown to converge upon grid refinement.

Figure 11 shows results calculated on a 4000-cell grid using the SW EOS, and the PR EOS with and without the model for the triple point and vapor–solid equilibrium behavior. Five pressure plateaux can be identified in Figure 11a. Apart from the initial pressure plateaux there are three intermediate plateaux, one at the saturation line, at approximately $1.75\,\text{MPa}$, one at the triple point ($0.518\,\text{MPa}$), and one apparently at the sublimation line, at approximately $0.3\,\text{MPa}$. In an examination of Figures 11b and 11e, it is seen that this pressure plateau is split between a left part at the sublimation line and a right part as a high-temperature vapor.
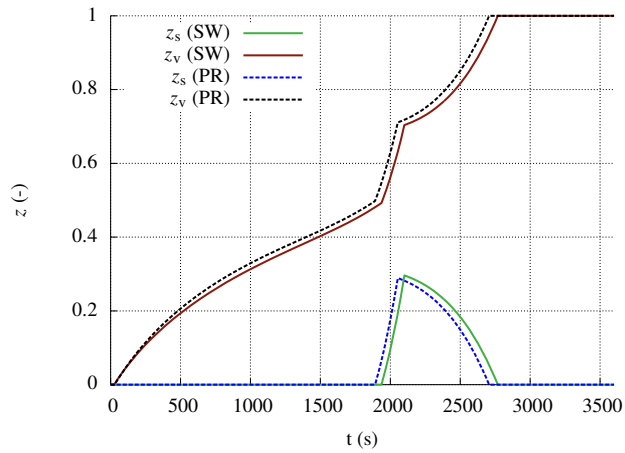
Regarding the different EOSs, two main effects can be seen in Figure 11. First of all, the SW EOS predicts a faster-moving liquid-phase rarefaction wave, seen on the left-hand side in Figure 11a. This is caused by the higher liquid speed of sound predicted by the SW EOS compared to the PR

26
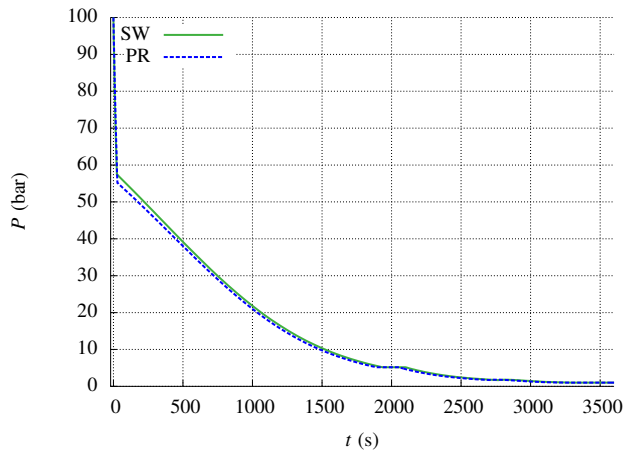
(a) Pressure
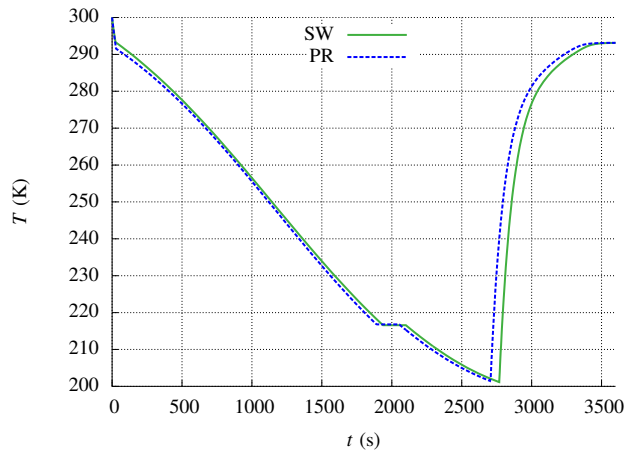
(b) Temperature

(c) Mass fractions

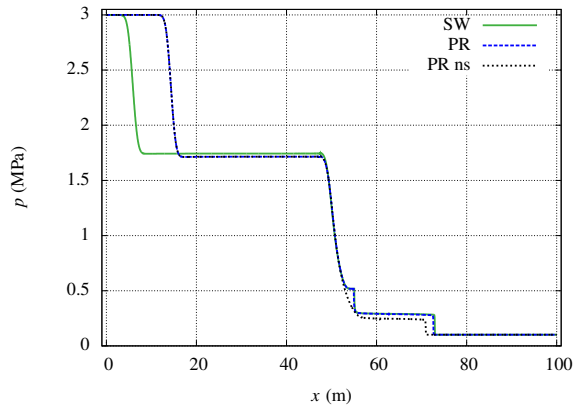Figure 10: Comparison of the Span–Wagner (SW) and Peng–Robinson (PR) EOS for the vessel simulation.

EOS, cf. Figure 5c. Second, the PR EOS without the solid model fails to predict the sublimation plateau, as seen in Figure 11c, and it underestimates the highest temperature by 13 K and the lowest temperature by 8 K, Figure 11b. This indicates that, in order to obtain accurate results, it is necessary to include solid formation in the model.

Depressurization of a pipe

We now consider a case in which the state will dynamically pass from single-phase to two-phase (vapor–liquid), three-phase (vapor–liquid–solid), and then to two-phase (vapor–solid). A closed pipe of length $100\,\text{m}$ is filled with CO_2 at a pressure of $10\,\text{MPa}$ and a temperature of $300\,\text{K}$. At time $t = 0$, the right-hand end is fully opened to atmospheric conditions, and expansion waves start traveling to the left. This is illustrated in Figure 12, where the SW EOS and a computational grid of 1000 cells have been employed. As in the previous section, the MUSCL-FORCE scheme was employed with the minmod limiter and a CFL number of 0.5. At $t = 5.5\,\text{s}$, practically the whole pipe is at the triple point. After that, the pressure decrease continues, with CO_2 in a vapor state with some solid.

The present case constitutes a challenging test regarding the robustness of the thermodynamic routines. It is also challenging for the numerical method employed to solve the fluid eqs 39–41, in particular, because of the strongly varying mixture speed of sound.

The case has also been calculated employing the PR EOS. A comparison between the results obtained using the SW and the PR EOSs is displayed in Figure 13 for time $t = 0.2\,\text{s}$. Appreciable differences can be noted in the pressure and the temperature. Compared to the SW reference EOS, the PR EOS gives too low pressure, temperature, and mixture density, and too slow decompression wave speed. It is interesting to note that, in the present case, the SW EOS predicts that the pipe is emptied faster than the PR EOS, while it was the other way around for the vessel in Figure 10. This is because the SW EOS gives a higher speed of sound, which influences the pressure propagation in the pipe, but which does not enter directly into the vessel model. The plot of the liquid volume fraction in Figure 13d illustrates that the fluid is in a single-phase state until about $x = 84\,\text{m}$, after
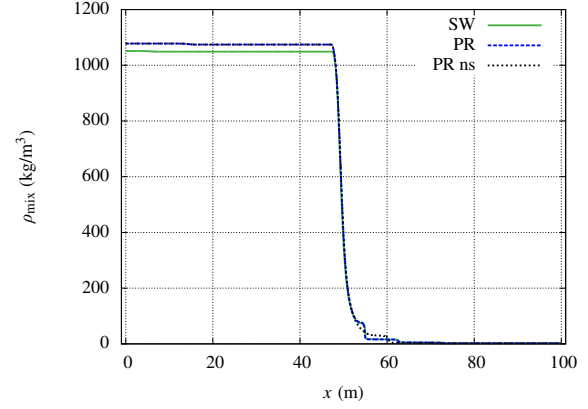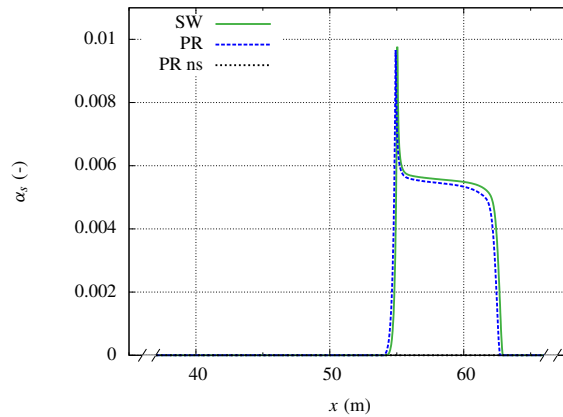
28
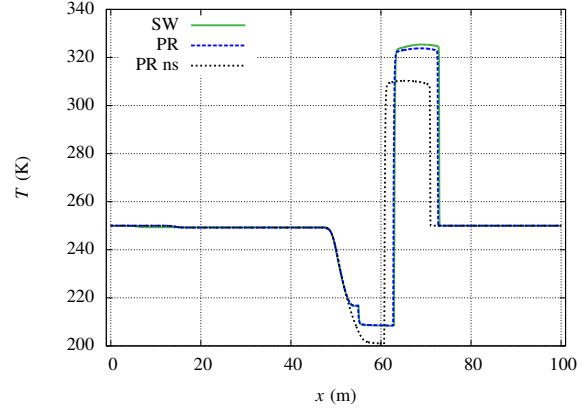
(a) Pressure

(b) Temperature
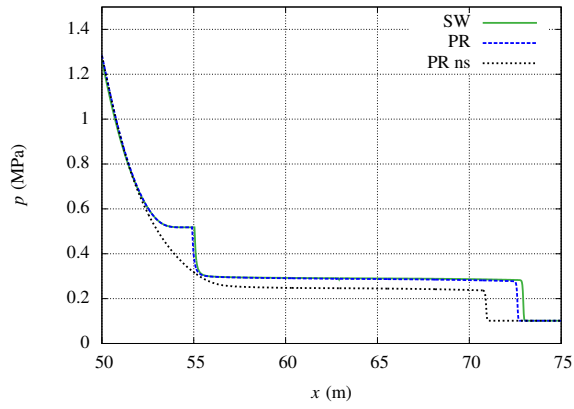
(c) Pressure, zoomed in

(d) Mixture density

(e) Solid volume fraction

Figure 11: Results for the shock tube at $t = 0.06$s. The Span–Wagner (SW) and Peng–Robinson (PR) EOS are compared, as well as the PR EOS without a solid model (labeled "PR ns"). 4000 grid cells.
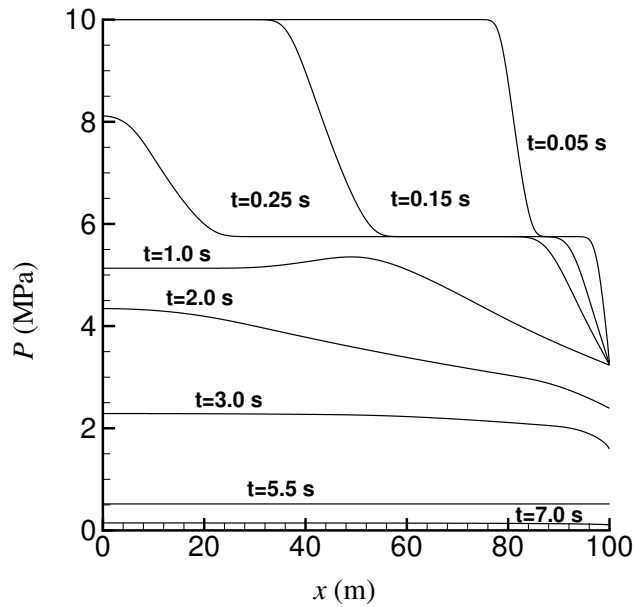
Figure 12: Single/two/three-phase depressurization of a pipe. Pressure profiles at various times. SW EOS, 1000 grid cells.

which phase change takes place.

The case is further illustrated in Figure 14 employing the SW EOS. Figure 14a shows the mixture speed of sound plotted together with the flow velocity. It can be seen that the flow is subsonic in the pipe. The speed of sound is equal to the single-phase liquid speed of sound in the liquid region. As the fluid enters the two-phase region, the speed of sound drops discontinuously. At the outlet, the flow velocity and speed of sound are equal, which means that the flow is choked. As shown in Figure 13d, the specific entropy is constant in the pipe. This is because no source terms are added to the governing equations.

Figure 15 displays results for time $t = 7.4$ s. At this time, the state in the pipe has passed the triple point. The differences between the SW and PR EOSs are now considerable. In particular, the pressure predicted by the SW EOS in Figure 15b has reached an atmospheric level, while the pressure predicted by the PR is still at at about 0.48 MPa. We have also included data calculated using the PR EOS without taking the solid formation into account (labeled "ns"). For the pressure and temperature in Figures 15b and 15c, this gives values lying between those calculated using the SW and PR EOSs when the solid is accounted for. This is since the solid formation retards the
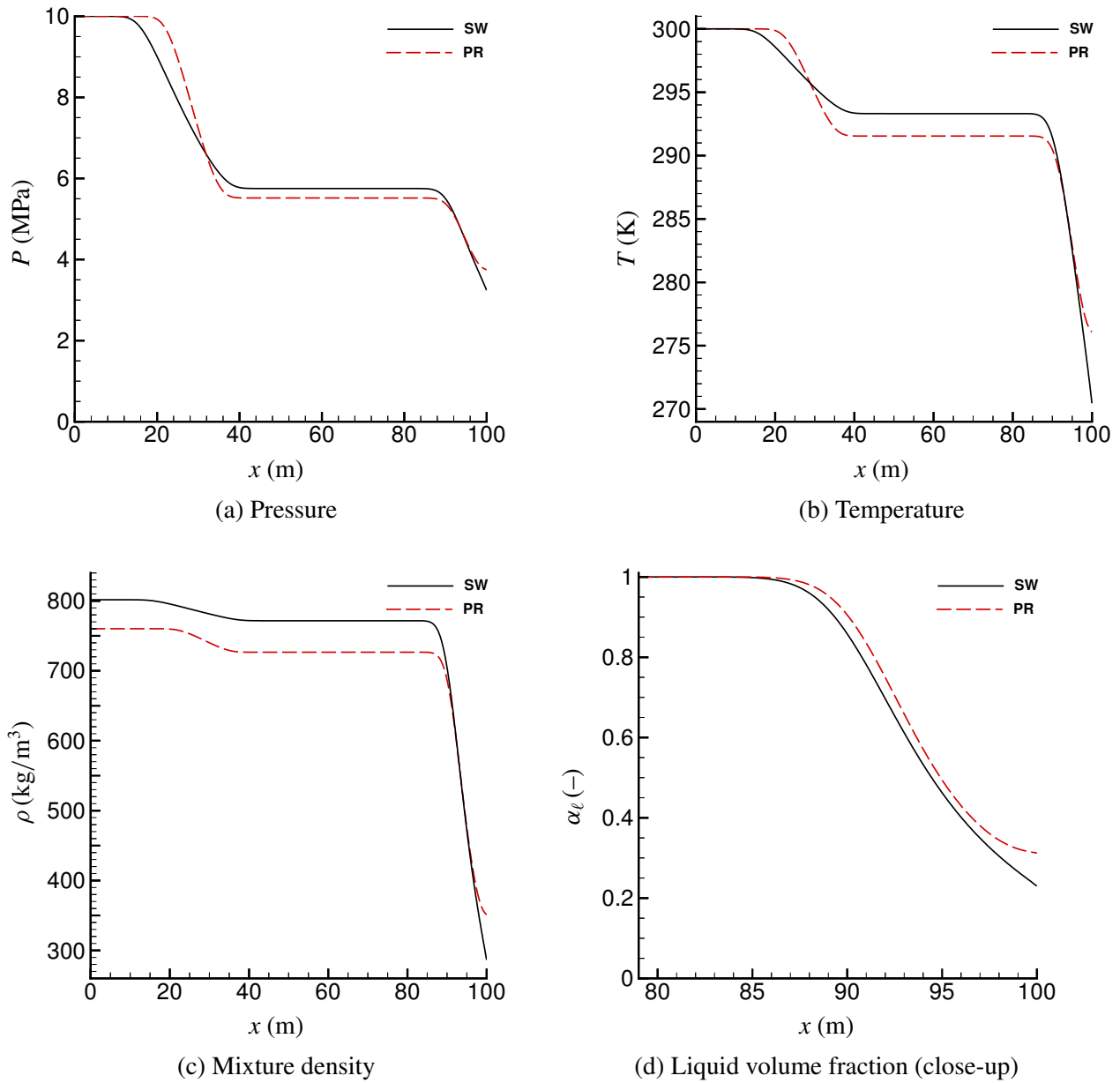
(a) Pressure

(b) Temperature

(c) Mixture density

(d) Liquid volume fraction (close-up)

Figure 13: Depressurization of a pipe. Calculations employing the Span–Wagner (SW) and Peng–Robinson (PR) EOS. Results at $t = 0.2\,\text{s}$. 1000 grid cells.
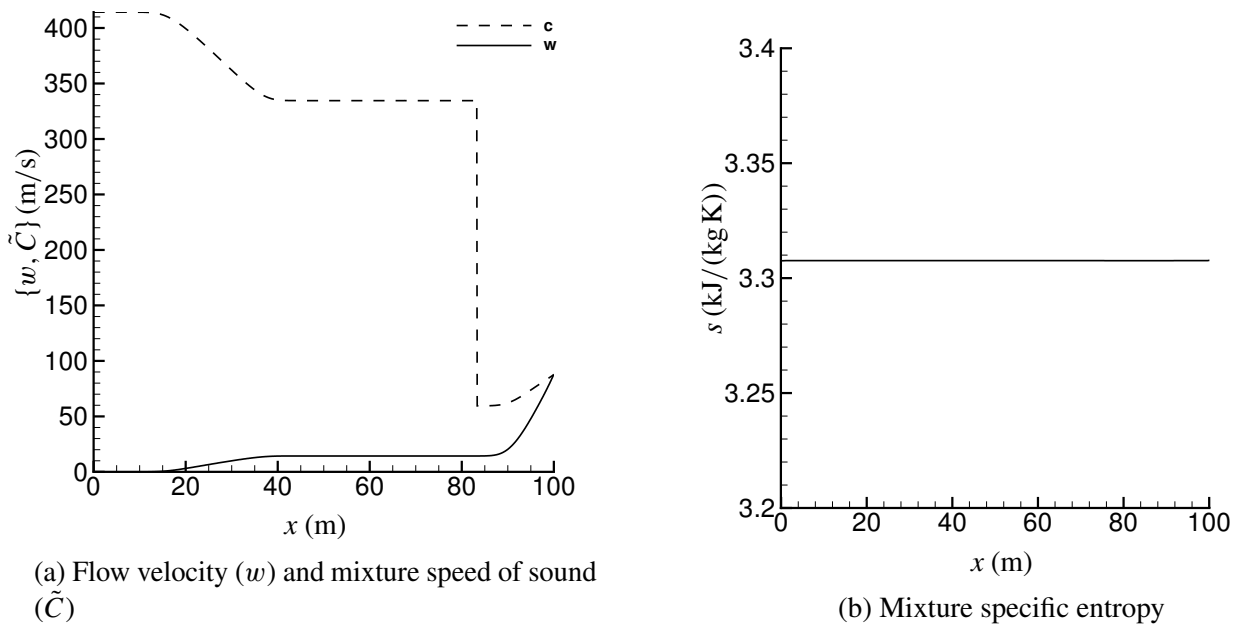
(a) Flow velocity (w) and mixture speed of sound ($\tilde{C}$)

(b) Mixture specific entropy

Figure 14: Depressurization of a pipe. Calculations employing the Span–Wagner (SW) EOS. Results at $t = 0.2\,\mathrm{s}$. 1000 grid cells.

depressurization of the fluid inside the pipe.

Conclusions

In this work, we have considered fluid-dynamics simulations of CO_2. In such simulations, the governing equations are commonly formulated such that it is natural to employ a density–energy state function. Furthermore, in depressurizations from elevated pressures to atmospheric conditions, it is necessary to account for the presence of dry ice. To do so, we have devised a method for handling solid–liquid–vapor CO_2 in conjunction with the Span–Wagner (SW) reference EOS. The method has been shown to be robust in challenging test cases. It therefore enables fluid-dynamics simulations with accurate CO_2 properties. To illustrate the effect of the EOS in fluid-dynamics simulations, we have compared results obtained using the SW EOS and the Peng–Robinson (PR) EOS. Since the thermodynamic variables are coupled through the fluid-dynamics governing equations, the EOS generally affects the whole simulation result. Our simulations have also indicated that failure
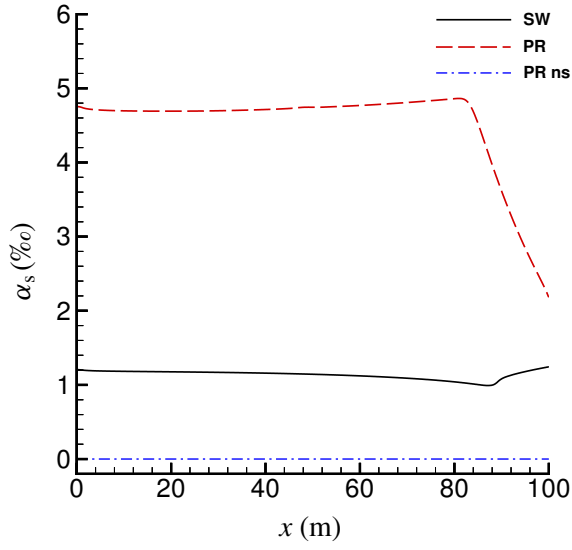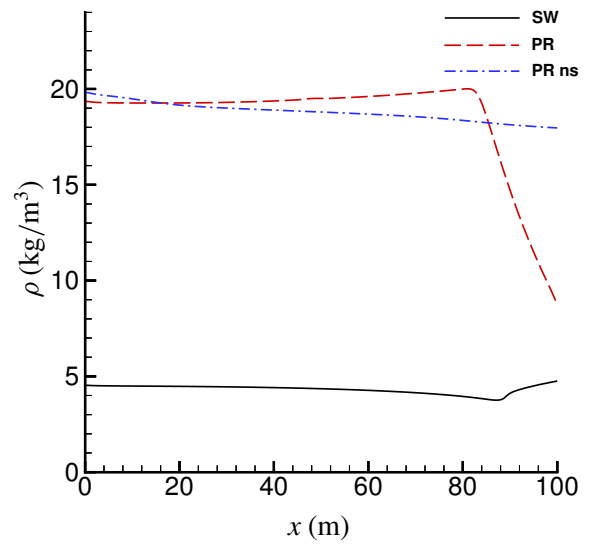
(a) Solid volume fraction
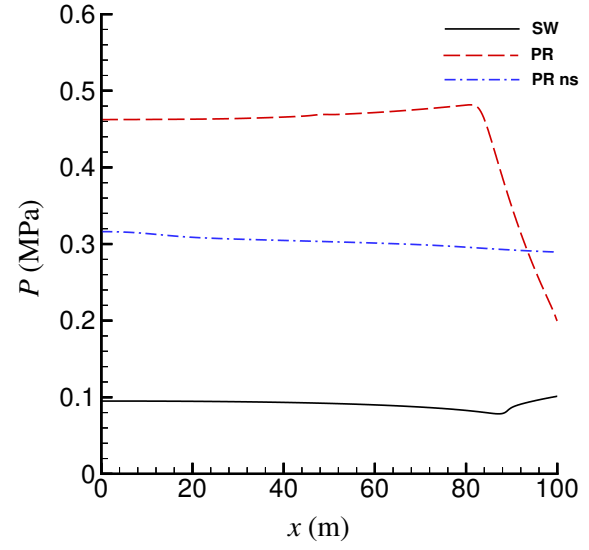
(b) Pressure
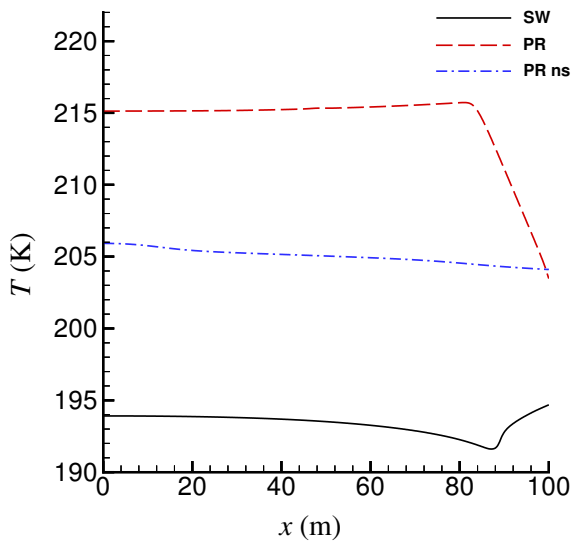
(c) Temperature

(d) Mixture density

Figure 15: Depressurization of a pipe. Calculations employing the Span–Wagner (SW) EOS, and the Peng–Robinson EOS with and without accounting for solid formation (PR and PR ns). Results at $t = 7.4\,\mathrm{s}$. 1000 grid cells.

to account for the formation of solid CO_2 may entail significant errors, even if the solid volume fraction is low.

Acknowledgement

References

1. International Energy Agency (IEA), *Energy Technology Perspectives*; 2012.

2. Aihara, S.; Misawa, K. Numerical simulation of unstable crack propagation and arrest in CO_2 pipelines. The First International Forum on the Transportation of CO_2 by Pipeline. Newcastle, UK, 2010.

3. Nordhagen, H. O.; Kragset, S.; Berstad, T.; Morin, A.; Dørum, C.; Munkejord, S. T. A new coupled fluid-structure modelling methodology for running ductile fracture. *Comput. Struct.* **2012**, *94–95*, 13–21.

4. Mahgerefteh, H.; Brown, S.; Denton, G. Modelling the impact of stream impurities on ductile fractures in CO_2 pipelines. *Chem. Eng. Sci.* **2012**, *74*, 200–210.

5. Aursand, E.; Aursand, P.; Berstad, T.; Dørum, C.; Hammer, M.; Munkejord, S. T.; Nordhagen, H. O. CO_2 pipeline integrity: A coupled fluid-structure model using a reference equation

of state for CO_2. GHGT-11 – 11th International Conference on Greenhouse Gas Control Technologies. Kyoto, Japan, 2012; To appear in Energy Procedia.

6. Aursand, P.; Hammer, M.; Munkejord, S. T.; Wilhelmsen, Ø. Pipeline transport of CO_2 mixtures: Models for transient simulation. *Int. J. Greenh. Gas Con.* **2013**, *15*, 174–185.

7. Michelsen, M. L. State function based flash specifications. *Fluid Phase Equilib.* **1999**, *158-160*, 617 – 626.

8. Giljarhus, K. E. T.; Munkejord, S. T.; Skaugen, G. Solution of the Span-Wagner equation of state using a density-energy state function for fluid-dynamic simulation of carbon dioxide. *Ind. Eng. Chem. Res.* **2012**, *51*, 1006–1014.

9. Gani, R.; Perregaard, J.; Johansen, H. Simulation strategies for design and analysis of complex chemical processes. *Chem. Eng. Res. Des.* **1990**, *68*, 407–417.

10. Flatby, P.; Lundström, P.; Skogestad, S. Rigorous dynamic simulation of distillation columns based on UV-flash. IFAC Symposium ADCHEM'94, Kyoto, Japan. 1994.

11. Eckert, E.; Kubícek, M. Modelling of dynamics for multiple liquid–vapour equilibrium stage. *Chem. Eng. Sci.* **1994**, *49*, 1783–1788.

12. Saha, S.; Carroll, J. J. The isoenergetic-isochoric flash. *Fluid Phase Equilib.* **1997**, *138*, 23–41.

13. Müller, D.; Marquardt, W. Dynamic multiple-phase flash simulation: Global stability analysis versus quick phase determination. *Comput. Chem. Eng.* **1997**, *21*, S817 – S822.

14. Gonçalves, F. M.; Castier, M.; Araújo, O. Q. F. Dynamic simulation of flash drums using rigorous physical property calculations. *Braz. J. Chem. Eng.* **2007**, *24*, 277–286.

15. Castier, M. Solution of the isochoric-isoenergetic flash problem by direct entropy maximization. *Fluid Phase Equilib.* **2009**, *276*, 7–17.

16. Arendsen, A. R. J.; Versteeg, G. F. Dynamic thermodynamics with internal energy, volume, and amount of moles as states: Application to liquefied gas tank. *Ind. Eng. Chem. Res.* **2009**, *48*, 3167–3176.

17. Wilhelmsen, Ø.; Skaugen, G.; Hammer, M.; Wahl, P. E.; Morud, J. C. Time efficient solution of phase equilibria in dynamic and distributed systems with differential algebraic equation solvers. *Ind. Eng. Chem. Res.* **2013**, *52*, 2130–2140.

18. Span, R.; Wagner, W. A new equation of state for carbon dioxide covering the fluid region from the triple-point temperature to 1100 K at pressures up to 800 MPa. *J. Phys. Chem. Ref. Data* **1996**, *25*, 1509–1596.

19. Lemmon, E. W.; Huber, M. L.; McLinden, M. O. NIST Standard Reference Database 23: Reference Fluid Thermodynamic and Transport Properties-REFPROP, Version 9.0, National Institute of Standards and Technology, Standard Reference Data Program. **2010**, Gaithersburg.

20. Peng, D. Y.; Robinson, D. B. A new two-constant equation of state. *Ind. Eng. Chem. Fund.* **1976**, *15*, 59–64.

21. Trusler, J. P. M. Equation of state for solid phase I of carbon dioxide valid for temperatures up to 800 K and pressures up to 12 GPa. *J. Phys. Chem. Ref. Data* **2011**, *40*, Article 043105.

22. Trusler, J. P. M. Erratum: Equation of state for solid phase I of carbon dioxide valid for temperatures up to 800 K and pressures up to 12 GPa [J. Phys. Chem. Ref. Data 40, 043105 (2011)]. *J. Phys. Chem. Ref. Data* **2012**, *41*, Article 039901.

23. Jäger, A.; Span, R. Equation of state for solid carbon dioxide based on the Gibbs free energy. *J. Chem. Eng. Data* **2012**, *57*, 590–597.

24. Höchst, *Properties of CO_2*; Pamphlet.

25. Dennis, J. E.; Schnabel, R. B. *Numerical Methods for Unconstrained Optimization and Nonlinear Equations*; Society for Industrial and Applied Mathematics (SIAM): Philadelphia, USA, 1996.

26. Petzold, L. R. *Description of DASSL: a differential/algebraic system solver*; Sandia National Laboratories, 1982; Tech. report SAND-82-8637.

27. Eggers, R.; Green, V. Pressure discharge from a pressure vessel filled with CO_2. *J. Loss Prevent. Proc.* **1990**, *3*, 59–63.

28. Gebbeken, B.; Eggers, R. Blowdown of carbon dioxide from initially supercritical conditions. *J. Loss Prevent. Proc.* **1996**, *9*, 285–293.

29. Toro, E. F.; Billett, S. J. Centred TVD schemes for hyperbolic conservation laws. *IMA J. Numer. Anal.* **2000**, *20*, 47–79.

30. Chen, G.-Q.; Toro, E. F. Centered difference schemes for nonlinear hyperbolic equations. *J. Hyperbolic Differ. Equ.* **2004**, *1*, 531–566.

31. Toro, E. F. MUSTA: A multi-stage numerical flux. *Appl. Numer. Math.* **2006**, *56*, 1464–1479.

32. Titarev, V. A.; Toro, E. F. MUSTA schemes for multi-dimensional hyperbolic systems: analysis and improvements. *Int. J. Numer. Meth. Fl.* **2005**, *49*, 117–147.

33. Munkejord, S. T.; Evje, S.; Flåtten, T. The multi-stage centred-scheme approach applied to a drift-flux two-phase flow model. *Int. J. Numer. Meth. Fl.* **2006**, *52*, 679–705.

34. Munkejord, S. T.; Jakobsen, J. P.; Austegard, A.; Mølnvik, M. J. Thermo- and fluid-dynamical modelling of two-phase multi-component carbon dioxide mixtures. *Int. J. Greenh. Gas Con.* **2010**, *4*, 589–596.

35. van Leer, B. Towards the ultimate conservative difference scheme V. A second-order sequel to Godunov's method. *J. Comput. Phys.* **1979**, *32*, 101–136.

36. Osher, S. Convergence of generalized MUSCL schemes. *SIAM J. Numer. Anal.* **1985**, *22*, 947–961.

37. Ketcheson, D. I.; Robinson, A. C. On the practical importance of the SSP property for Runge-Kutta time integrators for some common Godunov-type schemes. *Int. J. Numer. Meth. Fl.* **2005**, *48*, 271–303.

38. Flåtten, T.; Lund, H. Relaxation two-phase flow models and the subcharacteristic condition. *Math. Mod. Meth. Appl. S.* **2011**, *21*, 2379–2407.

39. Lund, H. A hierarchy of relaxation models for two-phase flow. *SIAM J. Appl. Math.* **2012**, *72*, 1713–1741.

40. LeVeque, R. J. *Finite Volume Methods for Hyperbolic Problems*; Cambridge University Press: Cambridge, UK, 2002.